J. Fluid Mech. (1978), *vol.* 85, *part* 1, *pp.* 57–83
Printed in Great Britain

Measurements and prediction of fully developed turbulent flow in an equilateral triangular duct

By A. M. M. ALY, A. C. TRUPP AND A. D. GERRARD
Department of Mechanical Engineering, University of Manitoba, Winnipeg, Canada

(Received 12 November 1976 and in revised form 29 June 1977)

Fully developed air-flows through an equilateral triangular duct of 12·7 cm sides were investigated over a Reynolds number range of 53 000 to 107 000. Based on equivalent hydraulic diameter, friction factors were found to be about 6 % lower than for pipe flow. Mean axial velocity distributions near the wall were describable by the inner law of the wall (when based on local wall shear stress) but the constants differ slightly from those for pipe flow. As expected, the secondary flow pattern was found to consist of six counter-rotating cells bounded by the corner bisectors. Maximum secondary velocities of about 1½ % of the bulk velocity were observed. The effects of secondary currents were evident in the cross-sectional distributions of mean axial velocity, wall shear stress and Reynolds stresses, and very prominent in the turbulent kinetic energy distribution. For the flow prediction, the vorticity production terms were expressed by modelling the Reynolds stresses in the plane of the cross-section in terms of gradients in the mean axial velocity and a geometrically calculated turbulence length scale. The experimental and predicted characteristics of the flow are shown to be in good agreement.

1. Introduction

Fully developed turbulent flows in straight non-circular ducts are helical in nature. The spiral motion is due to secondary currents which act in the plane normal to the channel walls and generate mean shear stresses to maintain equilibrium between Reynolds stresses and pressure gradients in the asymmetric cross-section. Secondary flows of this type are encountered in many turbulent flow geometries including triangular and rectangular ducts, eccentric annuli and parallel-flow rod bundles. The square duct has been studied the most extensively both experimentally (Nikuradse 1926; Hoagland 1960; Leutheusser 1963; Brundrett & Baines 1964; Gessner & Jones 1965; Launder & Ying 1972) and analytically (Launder & Singham 1971; Wilson, Azad & Trupp 1971; Launder & Ying 1973; Gerard 1974). Rectangular ducts have additionally been examined by Tracey (1965) and Hinze (1973). Other duct configurations which have been explored include, for example, an open triangular duct (Liggett, Chiu & Miao 1965), two square interconnected sub-channels (Lyall 1971) and a circular pipe with one or two eccentric rods (Kacker 1973). In recent years, rod bundles have received increasing attention, particularly from the nuclear power industry (e.g. Rowe, Johnson & Knudsen 1974; Rogers & Tahir 1975), since heat transfer is enhanced by secondary flows. However, there are still no reliable measurements of secondary flows in either square or triangular rod bundle arrays. The first attempt was apparently due to Hall & Svenningsson (1971) who used the triangular array facility of Kjellstrom &

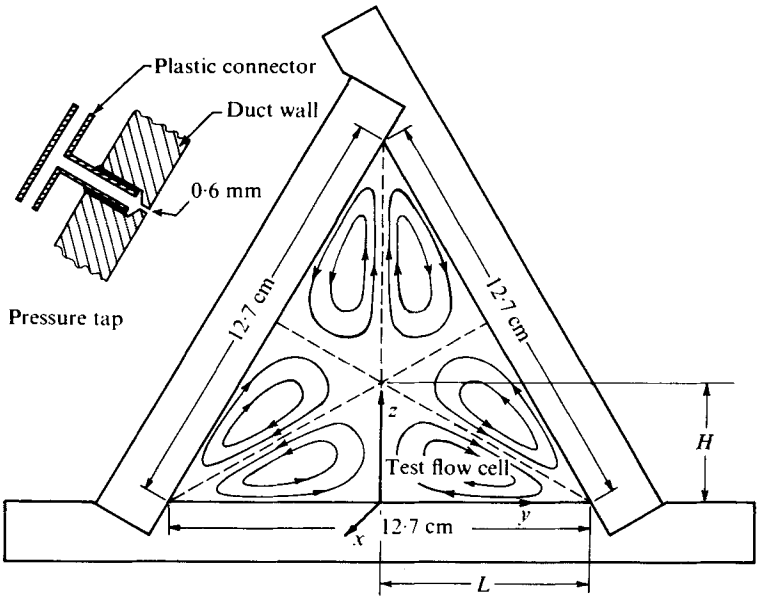

FIGURE 1. Cross-section of equilateral triangular test section.

Stenback (1970). Their results using a rotatable hot wire were not conclusive and they recommended further investigation. Similarly, although Trupp & Azad (1975) could infer the direction and approximate magnitude of secondary flows from momentum and energy balances, they were unable to measure the tiny secondary velocities via conventional X-probes and a three-wire probe in a simulated infinite triangular array. Carajilescov & Todreas (1976) have predicted mean axial velocity distributions and secondary flow fields for triangular arrays of rods with different aspect ratios. The predictions for axial velocity were in good agreement with experimental results obtained by laser-Doppler anemometry for one array; however, the predicted secondary velocities could not be verified since measurements were inadequate. The present *research evolved from a desire to test an equilateral triangular array of rods having* unity pitch-to-diameter ratio (i.e. rods touching). This limiting aspect ratio is the only one that can be practically constructed to truly constitute a member of the infinite array series where secondary flows are confined to within each symmetric part of the sub-channel. But a tricuspid channel is difficult to build accurately; hence the equilateral triangular duct was chosen for its similarity and simplicity, and the fact that triangular ducts have received little previous attention.

Nikuradse (1930) was the first to deal with turbulent flow in triangular ducts. He noted that lines of constant mean axial velocity (isovels) in these ducts tended to bulge towards the corners, and he confirmed the existence of secondary flows through flow visualization. Cremers & Eckert (1962) published measurements of mean axial velocity and five Reynolds stresses in an isosceles triangular duct with a vertex angle of about 12°. They reported that there was no experimental evidence of secondary flows at a Reynolds number of 10 900 although contour plots of axial velocity fluctuations strongly suggest the presence of secondary flows near the base. In a similar channel (vertex angle of 20°), at double the Reynolds number, Kokorev *et al.* (1971) detected three cells of secondary flow in each symmetric half of the channel. Other

experimental investigations involving triangular ducts have mainly concerned the transitional flow regime (e.g. Cope & Hanks 1972; Bandopadhayay & Hinwood (1973).

For fully developed turbulent flow in an equilateral triangular duct, the secondary flow pattern consists of six counter-rotating cells bounded by the corner bisectors. For each cell, the circulation is from the high momentum central core region to the corner region via the corner bisector, with return along the wall and mid-wall bisector (see figure 1). This secondary flow influences mean axial velocity ($\overline{U}$) and mean turbulent kinetic energy (k) distributions and acts to homogenize the local wall shear stress (τ). The experimental portion of the present research consisted of measurements of axial pressure drop, local wall shear stress, distributions of mean velocities ($\overline{U}$, $\overline{V}$, $\overline{W}$ in the x, y, z directions respectively) and five Reynolds stresses (not $\rho\overline{vw}$), and power spectra of axial velocity fluctuations (u) in the test flow cell of the geometry shown in figure 1. Measurements were conducted at Reynolds numbers, based on bulk velocity (U_b) and equivalent hydraulic diameter (D_h), of 53 000, 81 100 and 107 300. The experimental results presented and discussed here include some of the results documented by Gerrard (1976) as well as more recent refined measurements of Reynolds stresses and secondary velocities.

The analytical part of the research involved numerical prediction of the flow characteristics. Unlike the square duct, there has been essentially no previous work done on triangular ducts since the pioneering efforts of Deissler & Taylor (1959) which did not allow for secondary flows. The prediction of Kokorev *et al.* (1971) is limited to the wall shear stress distribution, whereas Gerard (1974) was unable to apply the finite-element technique owing to lack of experimental data as input. The prediction technique described here employed the general elliptic finite-difference procedure of Gosman *et al.* (1969) and adopted the fully modelling procedure outlined by Launder & Ying (1973). The predicted results are shown to be in good agreement with the experimental data.

2. Theoretical analysis for flow prediction

2.1. *General*

In the equilateral triangular duct, symmetry permits the flow cross-section to be subdivided into six primary flow cells. Each of these cells is identical when viewed with respect to rotated co-ordinate systems (except for handedness of secondary circulation), and no net mass, momentum or energy is transferred across any boundary. A knowledge of the flow properties in any one cell is therefore sufficient to describe the entire flow field. The primary flow cell and Cartesian co-ordinate system used in the present investigation are shown in figure 1. The conservation equations pertinent to flow prediction are outlined below for fully developed turbulent flow of a constant property fluid.

The Reynolds equations are:

y direction,

$$\rho\left(\overline{V}\frac{\partial\overline{V}}{\partial y}+\overline{W}\frac{\partial\overline{V}}{\partial z}\right)=-\frac{\partial P}{\partial y}+\mu\left(\frac{\partial^2\overline{V}}{\partial y^2}+\frac{\partial^2\overline{V}}{\partial z^2}\right)-\rho\left(\frac{\partial\overline{v^2}}{\partial y}+\frac{\partial\overline{vw}}{\partial z}\right); \tag{1}$$

z direction,

$$\rho\left(\overline{V}\frac{\partial\overline{W}}{\partial y}+\overline{W}\frac{\partial\overline{W}}{\partial z}\right)=-\frac{\partial P}{\partial z}+\mu\left(\frac{\partial^2\overline{W}}{\partial y^2}+\frac{\partial^2\overline{W}}{\partial z^2}\right)-\rho\left(\frac{\partial\overline{vw}}{\partial y}+\frac{\partial\overline{w^2}}{\partial z}\right); \tag{2}$$

x direction,

$$\rho\left(\overline{V}\frac{\partial\overline{U}}{\partial y}+\overline{W}\frac{\partial\overline{U}}{\partial z}\right)=-\frac{\partial P}{\partial x}+\mu\left(\frac{\partial^2\overline{U}}{\partial y^2}+\frac{\partial^2\overline{U}}{\partial z^2}\right)-\rho\left(\frac{\partial\overline{uv}}{\partial y}+\frac{\partial\overline{uw}}{\partial z}\right); \tag{3}$$

where u, v, w are the fluctuating velocity components in the x, y, z directions respectively, P is the mean static pressure, ρ and μ are the fluid density and dynamic viscosity, and the overbar designates time-averaging. Along the y axis (wall boundary) the convective terms and the y direction gradient terms vanish from the Reynolds equations owing to the no-slip condition. Along the corner bisector, $\overline{V}=-3^{\frac{1}{2}}\overline{W}$ since no net flow crosses the boundary. Along the z axis (normal to mid-wall), equation (1) must vanish since there can be no net momentum transfer in the y direction across this boundary. In fact, here, $\overline{V}=0$ everywhere so $\partial\overline{V}/\partial z=0=\partial^2\overline{V}/\partial z^2$, $\partial^2\overline{V}/\partial y^2=0$ since $\overline{V}$ has opposite signs on each side of the z axis, $\partial P/\partial y=0=\partial\overline{v^2}/\partial y$ owing to symmetry, hence it can be readily shown that $\overline{vw}=0$ along this boundary. On the other hand, on this same boundary, $\partial\overline{uv}/\partial y$ (like $\partial\overline{V}/\partial y$) may have finite values since $\overline{uv}$ (like $\overline{V}$) has an antisymmetric distribution about the z axis. For this reason and because $\overline{W}$ may have finite values along the z axis except at the wall and duct centreline, it is not possible to obtain a simple theoretical distribution for $\overline{uw}$ at this boundary from (3).

2.2. *The analytical model*

The stream function (ψ) is defined by

$$\rho\overline{V}=\partial\psi/\partial z,\quad \rho\overline{W}=-\partial\psi/\partial y. \tag{4}$$

The axial vorticity (ω) is defined by

$$\omega=\partial\overline{W}/\partial y-\partial\overline{V}/\partial z. \tag{5}$$

Substituting (4) into (5) yields

$$-\frac{\partial}{\partial y}\left(\frac{1}{\rho}\frac{\partial\psi}{\partial y}\right)-\frac{\partial}{\partial z}\left(\frac{1}{\rho}\frac{\partial\psi}{\partial z}\right)-\omega=0. \tag{6}$$

The pressure gradients in (1) and (2) may be eliminated by differentiating (1) with respect to z and (2) with respect to y, and subtracting one from the other. The result written in terms of ω and ψ is

$$\frac{\partial}{\partial y}\left(\omega\frac{\partial\psi}{\partial z}\right)-\frac{\partial}{\partial z}\left(\omega\frac{\partial\psi}{\partial y}\right)-\frac{\partial}{\partial y}\left[\frac{\partial(\mu\omega)}{\partial y}\right]-\frac{\partial}{\partial z}\left[\frac{\partial(\mu\omega)}{\partial z}\right]$$
$$-\rho\frac{\partial^2(\overline{v^2}-\overline{w^2})}{\partial y\,\partial z}+\rho\left(\frac{\partial^2\overline{vw}}{\partial y^2}-\frac{\partial^2\overline{vw}}{\partial z^2}\right)=0. \tag{7}$$

The vorticity and stream function (hence secondary velocities) fields for the triangular duct geometry may now be obtained by solving (6) and (7) providing the distributions of $\overline{v^2}$, $\overline{w^2}$ and $\overline{vw}$ can be described.

For the axial velocity prediction, by assuming the eddy viscosity (μ_t) to be locally isotropic, (3) may be rewritten as:

$$\rho\left(\overline{V}\frac{\partial\overline{U}}{\partial y}+\overline{W}\frac{\partial\overline{U}}{\partial z}\right)=-\frac{\partial P}{\partial x}+\frac{\partial}{\partial y}\left(\mu_e\frac{\partial\overline{U}}{\partial y}\right)+\frac{\partial}{\partial z}\left(\mu_e\frac{\partial\overline{U}}{\partial z}\right), \tag{8}$$

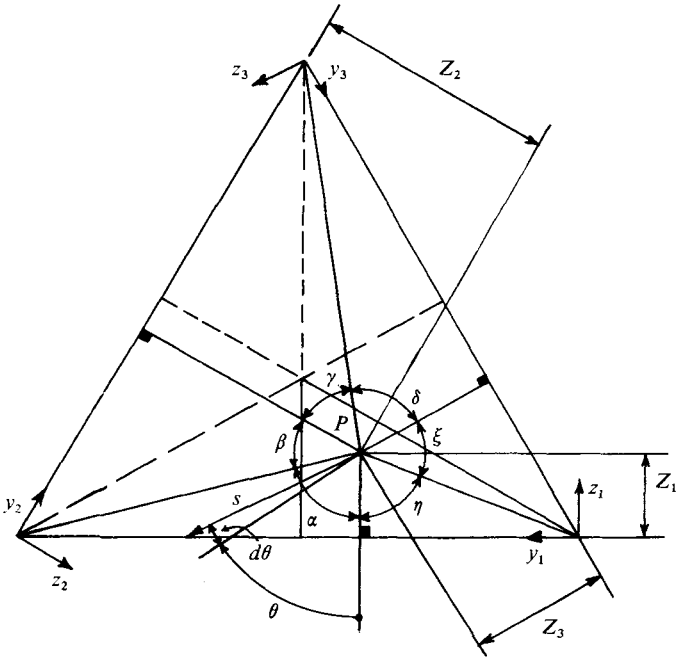

FIGURE 2. Notation for Buleev length scale calculation.

where the effective viscosity $\mu_e = \mu + \mu_t$. Substituting (4) into (8) yields:

$$\frac{\partial}{\partial y}\left(\overline{U}\frac{\partial \psi}{\partial z}\right) - \frac{\partial}{\partial z}\left(\overline{U}\frac{\partial \psi}{\partial y}\right) - \frac{\partial}{\partial y}\left(\mu_e \frac{\partial \overline{U}}{\partial y}\right) - \frac{\partial}{\partial z}\left(\mu_e \frac{\partial \overline{U}}{\partial z}\right) + \frac{\partial P}{\partial x} = 0. \tag{9}$$

This equation was used to obtain the mean axial velocity distribution based on the converged solution for the stream function.

Ideally, a numerical prediction scheme should require only basic specification of the flow, i.e. duct geometry, flow medium, and bulk velocity or Reynolds number. The prediction model was therefore selected so as to eliminate any empirical input. For the vorticity production terms in (7), Launder & Ying (1973) have rationalized, employing the following simple equations for the Reynolds stresses:

$$\overline{v^2} - \overline{w^2} = -cl^2\left[\left(\frac{\partial \overline{U}}{\partial y}\right)^2 - \left(\frac{\partial \overline{U}}{\partial z}\right)^2\right], \tag{10}$$

$$\overline{vw} = -cl^2\left(\frac{\partial \overline{U}}{\partial y}\right)\left(\frac{\partial \overline{U}}{\partial z}\right), \tag{11}$$

where c is an assignable constant and l is a turbulence length scale. The latter was calculated from the geometric formula suggested by Buleev (1963), namely:

$$\frac{1}{l} = \frac{1}{2}\int_0^{2\pi} \frac{d\theta}{S}, \tag{12}$$

where S is the distance from point P to the wall and angle θ is defined in figure 2.

Integrating (12) yielded:

$$\frac{1}{l} = \frac{1}{2Z_1}(\sin\alpha + \sin\eta) + \frac{1}{2Z_2}(\sin\beta + \sin\gamma) + \frac{1}{2Z_3}(\sin\delta + \sin\epsilon), \tag{13}$$

where the notation is explained in figure 2. The closed form (13) was used to calculate the turbulence length scale for each node.

By modelling the Reynolds stresses in (7) via (10) and (11), it was possible in principle to solve (6), (7) and (9) to obtain the flow characteristics. However, an eddy viscosity model was still required, and although this presented no substantial handicap, it was fundamentally preferable to employ the Prandtl–Kolmogorov formula:

$$\mu_t = \rho c_\nu (k)^{\frac{1}{2}} l, \tag{14}$$

which interrelates local values of eddy viscosity and turbulence length scale through the local mean turbulent kinetic energy $k \equiv \frac{1}{2}(\overline{u^2}+\overline{v^2}+\overline{w^2})$ and the proportionality constant c_ν. The rather widely used form:

$$\frac{\partial}{\partial y}\left(k\frac{\partial \psi}{\partial z}\right)-\frac{\partial}{\partial z}\left(k\frac{\partial \psi}{\partial y}\right)-\frac{\partial}{\partial y}\left[\left(\mu+\frac{\mu_t}{\sigma_k}\right)\frac{\partial k}{\partial y}\right]-\frac{\partial}{\partial z}\left[\left(\mu+\frac{\mu_t}{\sigma_k}\right)\frac{\partial k}{\partial z}\right]$$
$$-\mu_t\left[\left(\frac{\partial \overline{U}}{\partial y}\right)^2+\left(\frac{\partial \overline{U}}{\partial z}\right)^2\right]+\frac{\rho c_D (k)^{\frac{3}{2}}}{l}=0, \tag{15}$$

where σ_k is the effective Prandtl number for turbulent kinetic energy transport and c_D is a constant related to turbulent kinetic energy dissipation, was then used for the additional auxiliary equation for k. The final computation scheme required solutions to (6), (7) [with (10), (11) and (13)], (15) [with (13) and (14)], and (9) [with (13) and (14)]. Values used for the various constants were $c = 0{\cdot}006$, $c_\nu = 0{\cdot}22$, $\sigma_k = 1{\cdot}5$ and $c_D = 0{\cdot}39$. With the exception of c, these values were the same as those used by Launder & Ying (1973) for the square duct case ($c = 0{\cdot}010$).

The heat transfer characteristics of the flow were obtained by solving the enthalpy conservation equation which may be written as:

$$\frac{\partial}{\partial y}\left(\overline{H}\frac{\partial \psi}{\partial z}\right)-\frac{\partial}{\partial z}\left(\overline{H}\frac{\partial \psi}{\partial y}\right)=\frac{\mu}{\sigma_h}\left\{\frac{\partial^2 \overline{H}}{\partial y^2}+\frac{\partial^2 \overline{H}}{\partial z^2}\right\}-\rho\frac{\partial}{\partial y}\overline{hv}-\rho\frac{\partial}{\partial z}\overline{hw}, \tag{16}$$

where $\overline{H}$ and h represent the time average and fluctuating component of specific enthalpy respectively, and σ_h is the Prandtl number of the fluid. The turbulent enthalpy flux terms were approximated by:

$$-\overline{hv}=\frac{\mu_t}{\rho\sigma_{h,t}}\frac{\partial h}{\partial y}, \quad -\overline{hw}=\frac{\mu_t}{\rho\sigma_{h,t}}\frac{\partial h}{\partial z}, \tag{17}$$

where $\sigma_{h,t}$ is the turbulent Prandtl number, whose value was assumed equal to 0·9.

2.3. *Solution of the equations*

The general form of (6), (7), (9), (15) and (16) is:

$$A\frac{\partial}{\partial y}\left(\phi\frac{\partial \psi}{\partial z}\right)-A\frac{\partial}{\partial z}\left(\phi\frac{\partial \psi}{\partial y}\right)-\frac{\partial}{\partial y}\left[B\frac{\partial}{\partial y}(C\phi)\right]-\frac{\partial}{\partial z}\left[B\frac{\partial}{\partial z}(C\phi)\right]+D=0. \tag{18}$$

The new symbols in this standard elliptic form are identified for each equation in table 1. In order to solve the set of equations, an upwind finite-difference technique based on the general elliptic procedure of Gosman *et al.* (1969) was used with an irregular 31 × 31 Cartesian grid covering the same primary flow cell in which measurements were made (figure 1). The nodes were closely spaced near the wall and corner region where

Equation	ϕ	A	B	C	D
6	ψ	0	$1/\rho$	1	$-\omega$
7	ω	1	1	μ	$\rho\frac{\partial^2}{\partial y\,\partial z}\left\{cl^2\left[\left(\frac{\partial\bar{U}}{\partial y}\right)^2-\left(\frac{\partial\bar{U}}{\partial z}\right)^2\right]\right\}$ $-\rho\frac{\partial^2}{\partial y^2}\left[cl^2\left(\frac{\partial\bar{U}}{\partial y}\right)\left(\frac{\partial\bar{U}}{\partial z}\right)\right]+\rho\frac{\partial^2}{\partial z^2}\left[cl^2\left(\frac{\partial\bar{U}}{\partial y}\right)\left(\frac{\partial\bar{U}}{\partial z}\right)\right]$
9	$\bar{U}$	1	$\mu+\mu_t$	1	$\partial P/\partial x = 4\tau_w/D_h$
15	k	1	$\mu+\frac{\mu_t}{\sigma_k}$	1	$-\mu_t\left[\left(\frac{\partial\bar{U}}{\partial y}\right)^2+\left(\frac{\partial\bar{U}}{\partial z}\right)^2\right]+\frac{\rho c_D(k)^{\frac{3}{2}}}{l}$
16	$\bar{H}$	1	$\mu/\sigma_h+\mu_t/\sigma_{h,t}$	1	0

Note: τ_w is the average wall shear stress.

TABLE 1

the variables have steep gradients. Nodes on the corner bisector boundary were achieved by maintaining the spacing of nodes in the two directions in the ratio of $3^{\frac{1}{2}}:1$.

Regarding boundary conditions, the stream function is constant along all three boundaries; this constant was conveniently taken to be zero. The vorticity is zero at the two symmetry line boundaries. Near the solid wall, the vorticity was assumed to vary linearly with normal distance from the wall. Along the corner and mid-wall bisectors, the normal-to-boundary gradients of the mean axial velocity, turbulent kinetic energy and enthalpy were set to zero as is demanded by symmetry. A boundary condition for mean axial velocity was imposed on the first string of nodes in the fluid immediately adjacent to the wall. The grid was designed to have these nodes located beyond the viscous sublayer for the Reynolds number range involved. The $\bar{U}$ boundary condition was the familiar form:

$$\bar{U} = (\tau/\rho)^{\frac{1}{2}}[2{\cdot}5\ln(7{\cdot}69z^+)], \tag{19}$$

where z^+ is the dimensionless distance from the wall defined as

$$z^+ = \frac{z(\tau/\rho)^{\frac{1}{2}}}{\nu}, \tag{20}$$

where ν is the kinematic viscosity. A boundary condition for turbulent kinetic energy was also imposed at these same nodes. This was of the form:

$$k = \tau/(\rho^2 c_\nu c_D)^{\frac{1}{2}}, \tag{21}$$

the same as that used by Launder & Ying (1973).

In the solution procedure, continuously updated values of τ were used within the main iterative procedure. After each iteration step, local values of wall shear stress were computed at the second string of nodes from:

$$\bar{U} = \frac{(\tau/\rho)}{(c_\nu c_D)^{\frac{1}{2}}(k)^{\frac{1}{2}}}[2{\cdot}5\ln(7{\cdot}69z\,(c_\nu c_D)^{\frac{1}{4}}(k)^{\frac{1}{2}}/\nu)], \tag{22}$$

using the current computed values of $\bar{U}$ and k. The new τ values were then used to revise the $\bar{U}$ and k boundary conditions via (19) and (21) before embarking on the next

step. It is noted that a similar boundary condition technique has been previously employed by Gosman & Pun (1974).

The heat transfer field for the flow was solved at different Reynolds numbers for the case of a uniform average circumferential heat flux along the duct, and a uniform circumferential temperature distribution at any station. A semi-logarithmic boundary condition law for the enthalpy was imposed on the first string of nodes in the fluid. This was of the form:

$$\bar{H} - \bar{H}_w = \frac{\dot{q}'' \sigma_{h,t}}{(\rho\tau)^{\frac{1}{2}}} \left[\bar{U} \Big/ \left(\frac{\tau}{\rho}\right)^{\frac{1}{2}} + P^* \right], \tag{23}$$

where $\bar{H}_w$ is the mean specific enthalpy of the fluid at the wall, $\dot{q}''$ is the wall heat flux, and P^* is the Jayatilleke (1969) 'p function' which accounts for the enhanced resistance to heat or mass transfer offered by the viscous sublayer and is given by:

$$P^* = 9{\cdot}24[(\sigma_h/\sigma_{h,t})^{\frac{3}{4}} - 1]. \tag{24}$$

3. Experimental facility and equipment

3.1. *Wind tunnel*

The wind tunnel portion of the present facility was that used previously by Trupp & Azad (1975) in their investigation of rod bundle flow. For the present work, the wind tunnel was modified to operate in the open-circuit mode. Following the fan section, air passed through a diffuser, two sets of turning vanes, a screen section, and a circular contraction cone before entering a transition section. In this section, the flow area was gradually reduced and transformed to match the cross-section of the triangular test section. Air discharged from the open end of the triangular duct.

3.2. *Test section*

The triangular test section consisted of a 7·32 m wooden entrance length followed by a precision acrylic section. The overall length of the duct was 9·76 m and the length of the interior side walls was 12·70 cm. An interlocking construction as illustrated in figure 1 was used for both sections. It is estimated that variations in the side-wall lengths were less than $\pm$ 0·25 mm and $\pm$ 1·0 mm for the acrylic and wooden sections respectively.

Provision for axial pressure gradient measurements was made by locating static taps (figure 1) at 15·24 cm intervals along the duct length. The test plane for mean velocity and turbulence measurements was located about 133 equivalent hydraulic diameters from the test-section inlet, and 2·5 cm from the end of the triangular duct. Gerrard (1976) found that end effects were negligible at this position.

3.3. *Traversing mechanism*

Accurate positioning of either a Pitot tube or a hot-wire probe in the test plane was achieved by using a traversing mechanism having three orthogonal directions of motion. Vertical motion (z direction) was achieved by means of a DISA 55H01 traversing mechanism. This mechanism was mounted on two vernier callipers which allowed up to 15 cm of horizontal travel in the test plane. Motion in the axial direction was provided by two concentric tubes. The hot-wire probe could also be rotated con-

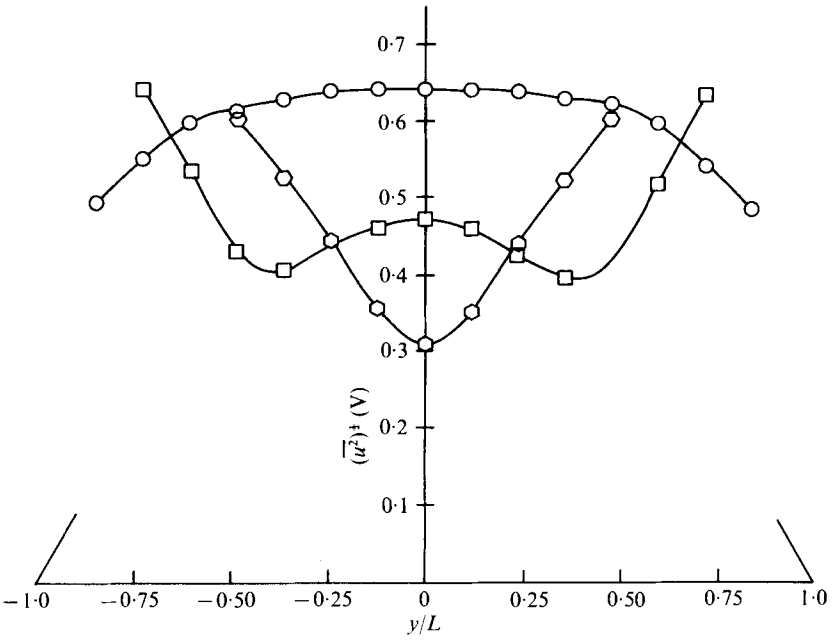

FIGURE 3. Distributions of $(\overline{u^2})^{\frac{1}{2}}$ along horizontal traverses in triangular duct. ○, $z/H = 0{\cdot}056$; □, $z/H = 0{\cdot}195$; ⬡, $z/H = 0{\cdot}333$.

centrically by turning the probe support, and this angular rotation was gauged using a small acrylic protractor fixed to the support.

The absolute position of the probe in the y direction was made by visual alignment of the probe with a scriber mark on the test-section base which located the mid-wall bisector. Probes were located in the z direction by observing their images as they were brought into contact with the shiny acrylic wall. The distance between the active section of a hot-wire probe and the wall was measured with a travelling microscope. It was estimated that absolute probe positions could be determined to within $\pm 0{\cdot}05$ mm and $\pm 0{\cdot}1$ mm in the vertical and horizontal directions respectively. The relative positional accuracy was of course much better since resolutions were 0·01 mm in the z direction and 0·02 mm in the y direction.

3.4. *Instrumentation*

Two Pitot tubes, with outside diameters of 1·067 mm and 1·27 mm, were constructed from stainless steel tubing having inside to outside diameter ratios of 0·6. Mean axial velocity and wall shear stress measurements at the highest Reynolds number were made with the large Pitot tube used in conjunction with a Betz projection manometer. This manometer had a range of 0–400 mm H_2O and an accuracy of $\pm 0{\cdot}05$ mm H_2O. A Fuess manometer (DISA 134B) and the smaller probe were used at the lower Reynolds numbers. The Fuess manometer had five ranges varying from 0–16 mm H_2O to 0–160 mm H_2O and an accuracy of $\pm 0{\cdot}5$ % of full scale.

Turbulence measurements were made using constant-temperature linearized hot-wire anemometry. The anemometry systems were manufactured by DISA and consisted of two sets of 55M10 anemometers with 55D10 linearizers and 55D25

Reynolds number	Centreline velocity $\bar{U}$ (m/s)	Average velocity U_b (m/s)	Friction velocity u^* (m/s)	Pressure drop dP/dx (N/m^3)
53000	14·4	11·5	0·570	20·3
81100	22·0	17·8	0·834	43·5
107300	28·4	23·2	1·05	70·3

TABLE 2. Nominal test conditions.

auxiliary units. These systems were operated in conjunction with DISA probes having 1·25 mm sensing lengths of 5 μm diameter platinum-plated tungsten wire. The ancillary equipment consisted of a 55D31 digital d.c. voltmeter, two 55D35 r.m.s. voltmeters, a 55D71 dual summing unit, and a 55D70 correlator.

Measurements of axial velocity fluctuations were made with a 55P01 single-wire probe with the sensing wire normal to the main flow and parallel to the test-section base. The data presented in this paper on Reynolds stresses and secondary velocities were obtained using a miniature 55P61 X-array probe. Values for $\overline{V}$ were checked using a rotatable 55P12 miniature 45° slanting probe. All hot-wire probes were calibrated *in situ* with the probe located at the duct centreline. A static calibration for the DISA M system consisted, for example for Re = 53 000, of typically 14 points over the range of about 8 m/s to 18 m/s with a correlation coefficient of 0·9997 for the straight line least-squares fit.

4. Experimental results and discussion

4.1. *General*

Prior to undertaking detailed measurements, the apparatus was investigated thoroughly for flow symmetry at both mean velocity and turbulence levels. A typical result is shown in figure 3. This and other results documented and discussed by Gerrard (1976) indicated that the flow at the test station was, for all practical purposes, symmetric. The importance of having achieved this condition is obvious. It in turn also meant that comprehensive measurements could be confined to one primary flow cell.

Detailed measurements were subsequently conducted at each of the three nominal test conditions outlined in table 2 where the average friction velocity (u^*) is $(\tau_w/\rho)^{\frac{1}{2}}$. The bulk velocities were obtained by numerical integration of the mean axial velocity fields. Both Pitot tube and hot-wire measurements were made at 150 locations constituting the nodes of a grid covering the test flow cell. This grid was regular except for additional points near the wall, and included points on the symmetry line boundaries.

4.2. *Friction factor*

The axial pressure distribution at each of the three test Reynolds numbers was determined from measurements at 64 static pressure taps spanning the length of the test section. The normalized distributions, referenced to the test plane, are shown in figure 4 together with straight lines faired through the data for comparison. No marked entrance region is evident.

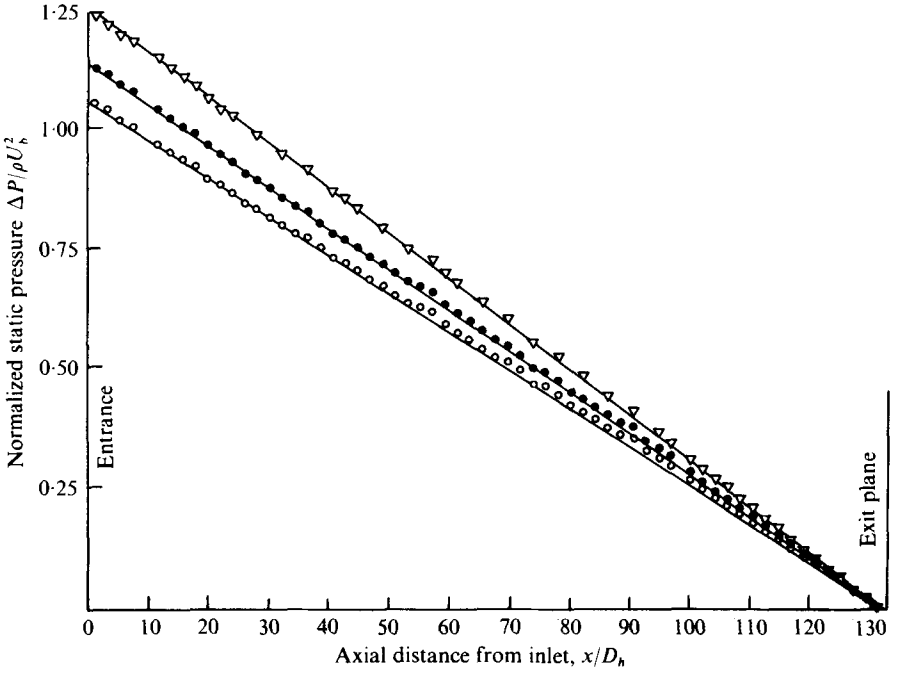

FIGURE 4. Static pressure distribution along duct axis.
▽, Re = 53000; ●, Re = 81100; ○, Re = 107300.

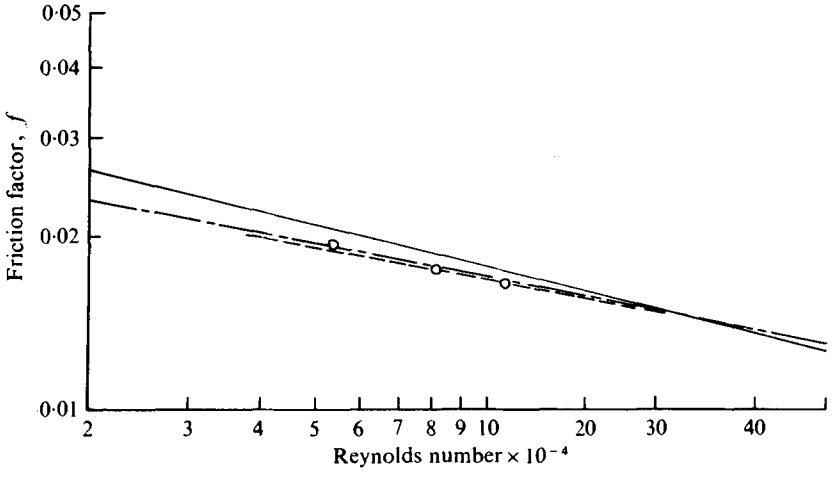

FIGURE 5. Friction factor *vs.* Reynolds number in equilateral triangular duct. ○, present experimental data; - - - -, present prediction; — · —, $f = 0{\cdot}184(K_\tau)^{1{\cdot}2}\, Re^{-0{\cdot}2}$, $K_\tau = 0{\cdot}936$, Malak *et al.* (1975); ——, $f = 0{\cdot}316Re^{-0{\cdot}25}$, Blasius.

The fully developed axial pressure gradient for each Reynolds number was determined from a least-squares fit straight line to the data from the last 16 downstream taps. Friction factors (f) were then computed as $D_h(-\partial P/\partial x)/\frac{1}{2}\rho U_b^2$ to an accuracy estimated to be within 3 %. These friction factors were found to be from 5 to 6½ % lower than values predicted by the Blasius correlation for friction factors in smooth circular tubes. Similar deviations have been reported for other non-circular ducts, e.g.

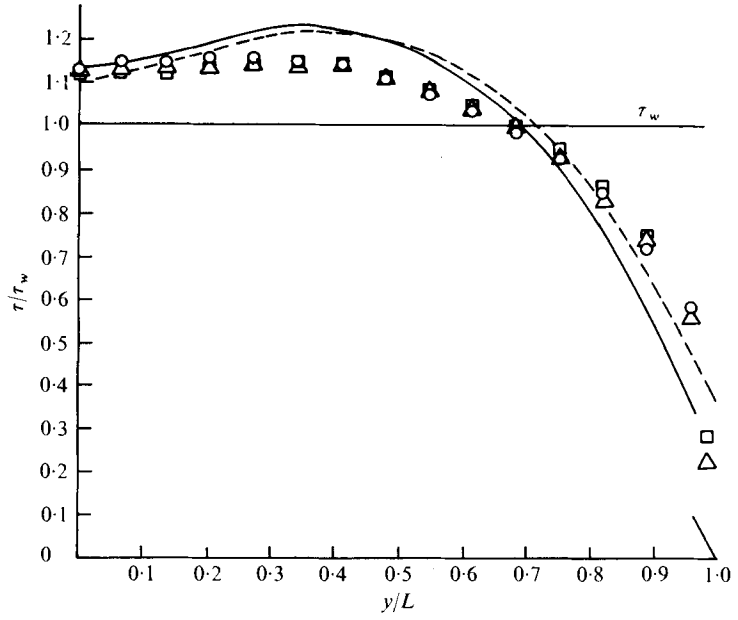

FIGURE 6. Local wall shear stress distributions. Present experimental data: ○, Re = 53000; △, Re = 81100; □, Re = 107300. Present prediction: ——, Re = 53000; - - - -, Re = 150000.

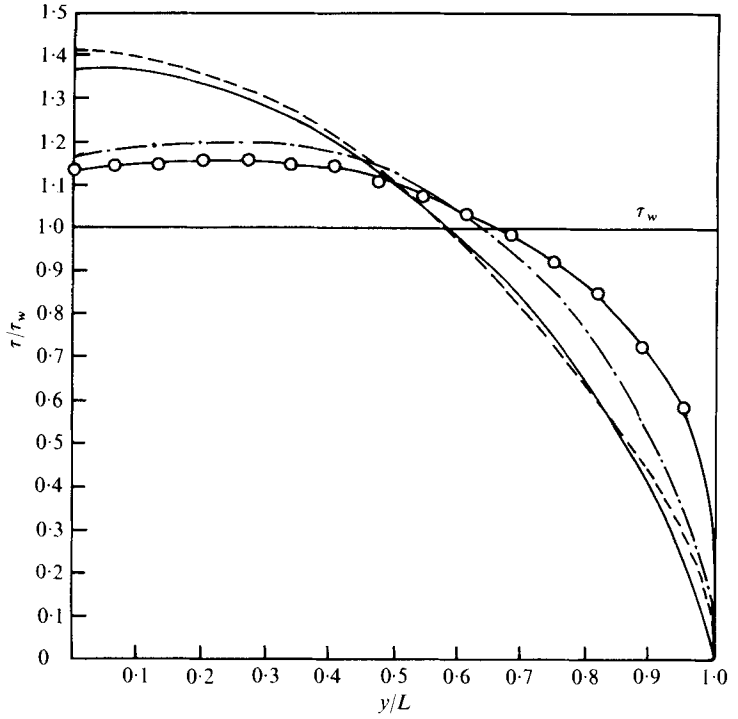

FIGURE 7. Comparison of measured and calculated wall shear stress distributions. —○—○—, present experimental data, Re = 53000, $u^*D_h/4\nu$ = 651; —·—·—, Kokorev *et al.* (1971) with allowance for secondary flow; ——, Gerard (1974), $u^*D_h/4\nu$ = 500, no allowance for secondary flow; - - - -, Deissler & Taylor (1959), Re = 24000 or 900000, no allowance for secondary flow.

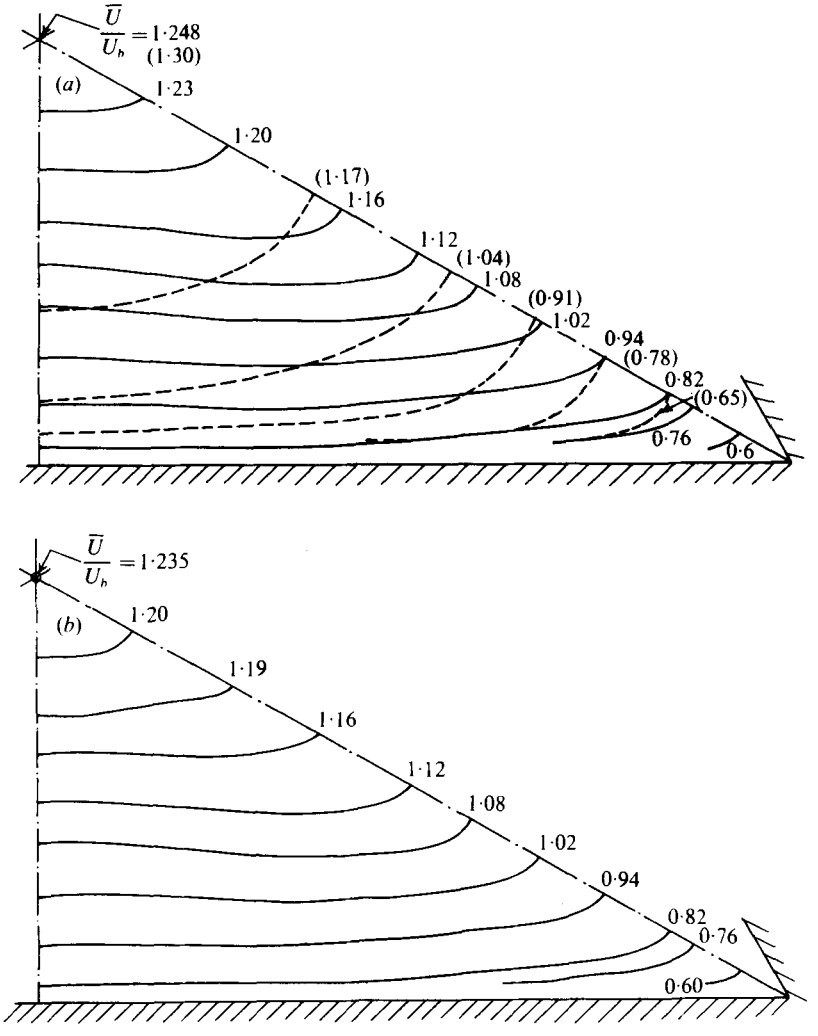

FIGURES 8(*a*, *b*). For legend see next page.

by Leutheusser (1963) for square ducts, and Carlson & Irvine (1961) for isosceles triangular ducts. Figure 5 illustrates the above deviation together with a correction for the inadequacies in the equivalent hydraulic diameter concept which has been suggested by Malak, Hejna & Schmid (1975). This correction which includes a geometrical factor in the correlation of friction factor and Reynolds number data gives a good representation of the present limited data.

4.3. *Local wall shear stress*

Local wall shear stress distributions for the test flow cell were determined by the Preston technique using the appropriate correlation of Patel (1965). The measured distributions of the axial component of wall shear stress at the three Reynolds numbers are shown in figure 6 after normalization by their integrated values. The distributions are qualitatively similar to those for rectangular ducts. Peak values are shifted

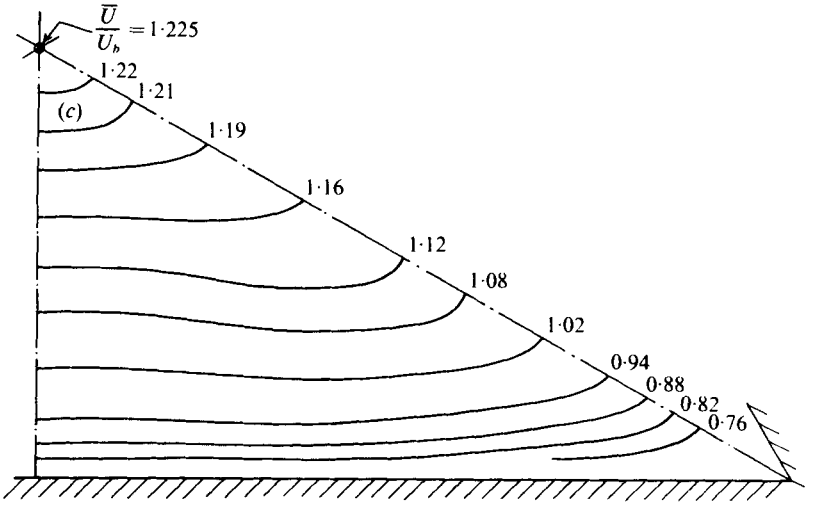

FIGURE 8. Isovel plots in primary flow cell. (*a*) ——, from present experimental data, $Re = 53\,000$, $u^*D_h/4\nu = 651$; - - - -, Gerrard (1974), $u^*D_h/4\nu = 500$, isovel values are bracketed. (*b*) $Re = 81\,100$. (*c*) $Re = 107\,300$.

towards the corner and, as shown by figure 7, this is contrary to predictions which do not allow for the secondary flows such as those presented by Deissler & Taylor (1959) and Gerard (1974), but similar to the predictions of Kokorev *et al.* (1971) who allowed for the secondary flow. This behaviour can undoubtedly be attributed to the tendency of the secondary flow to equalize wall shear stress around the perimeter of the channel.

4.4. *Mean axial velocities*

Mean axial velocity distributions were measured at the test station by a Pitot tube for three tunnel speeds. All mean velocity calculations were based on actual properties in the tunnel and included density corrections for variations in relative humidity. No corrections were made for velocity gradient or turbulence effects on the Pitot tube; however, the wall proximity correction suggested by Ower & Pankhurst (1966) was applied. Excluding turbulence effects, it is estimated that the experimentally derived mean velocities are accurate to within ± 1 %, while the estimated accuracy of the bulk velocity is ± 2 %. The isovels presented in figures 8(*a*)(*b*), and (*c*) have been normalized by the bulk velocities. These distributions are somewhat Reynolds number dependent; most noticeably near the duct centreline where the normalized local velocities decrease with increasing bulk velocity. At higher Reynolds number, the isovels also extend farther into the corners. The distortion of isovels caused by the secondary flows is remarkable. This is clear by comparing (figure 8*a*) the measured distribution with the pattern predicted by Gerrard (1974) for an equilateral triangular duct without secondary flows. This also indicates that secondary flows tend to decrease the velocity in the mid-wall regions and increase the velocity in the corner regions. Similar behaviour is shown later in conjunction with flow prediction.

The inner law of the wall is well known to apply to pipe, boundary-layer and rectangular-duct flows, albeit with minor variations in the values of the two empirical

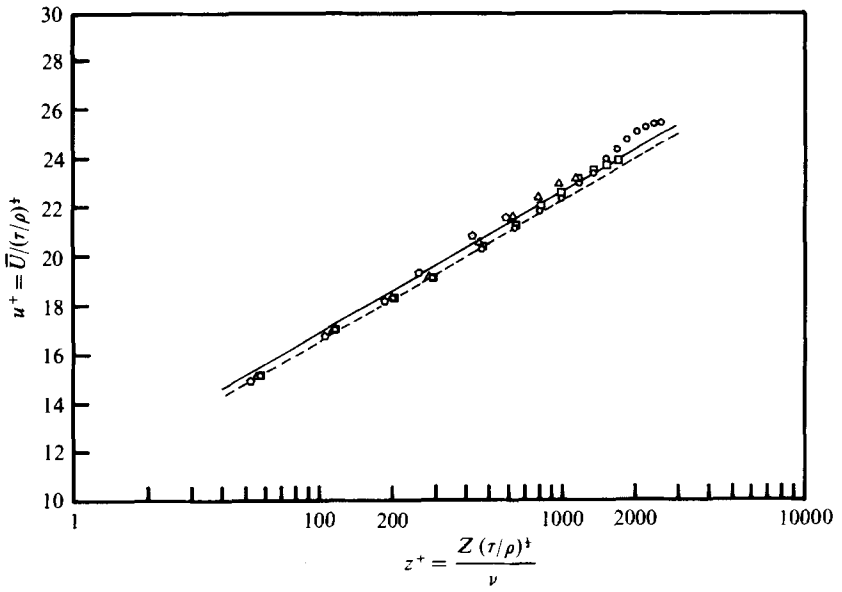

FIGURE 9. Mean velocity distribution in inner law co-ordinates based on local friction velocity. Re = 107300. Present experimental data: ○, y/L = 0·0; □, y/L = 0·409; △, y/L = 0·614; ⬠, y/L = 0·818; - - - -, equation (25); ——, rectangular duct, Leutheusser (1963),

$$u^+ = 2{\cdot}46 \ln z^+ + 5{\cdot}51.$$

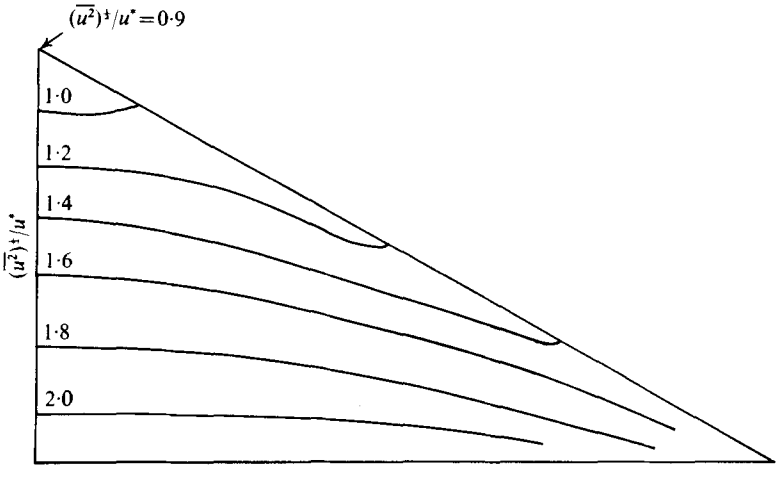

FIGURE 10. Contour plot of $(\overline{u^2})^{\frac{1}{2}}/u^*$ distribution. Re = 53000.

constants.† This same situation was found to apply also to the equilateral triangular duct. Correlations involving average friction velocity showed (as might be expected) considerable scatter, whereas correlations based on local friction velocity entailed relatively small standard deviations (Gerrard 1976). The latter is illustrated in figure 9. The least-squares fit of the 44 data points was:

$$u^+ = 2{\cdot}47 \ln z^+ + 5{\cdot}08, \tag{25}$$

† True universality of the constants perhaps exists only for a particular z^+ range for each flow since the upper limit on z^+ probably varies with the type of flow.

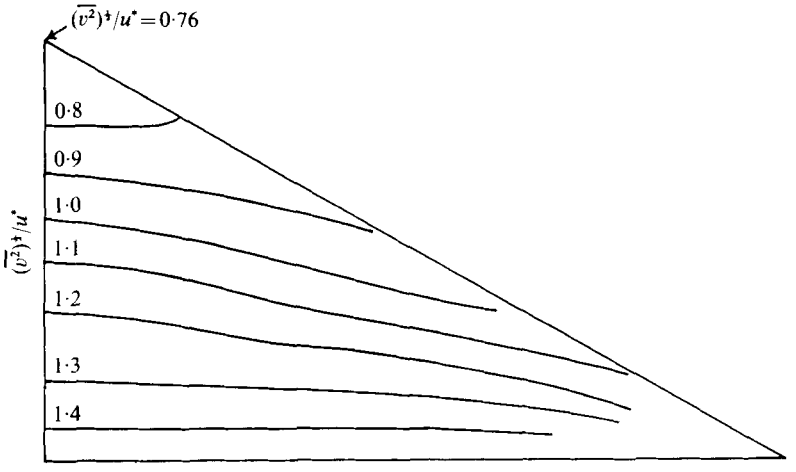

FIGURE 11. Contour plot of $(\overline{v^2})^{\frac{1}{2}}/u^*$ distribution. Re = 53000.

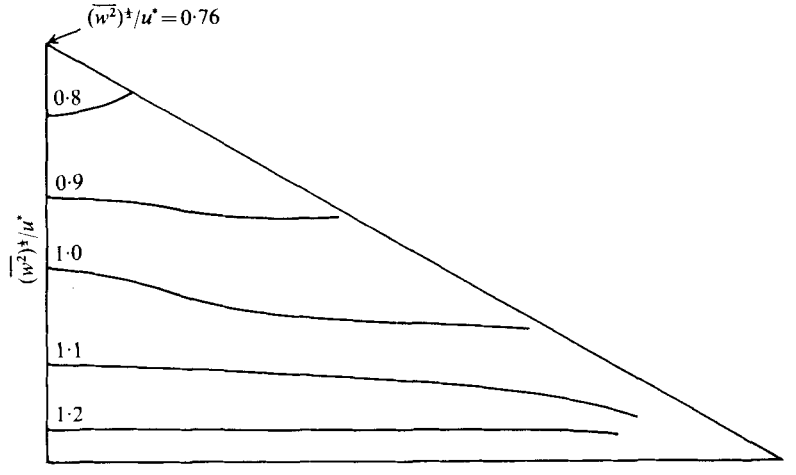

FIGURE 12. Contour plot of $(\overline{w^2})^{\frac{1}{2}}/u^*$ distribution. Re = 53000.

where $u^+ = \overline{U}/(\tau/\rho)^{\frac{1}{2}}$ is the non-dimensional mean axial velocity based on local friction velocity. This equation is plotted in figure 9 for comparison with the experimental data and the correlation for rectangular ducts due to Leutheusser (1963). The extent of the logarithmic distribution is reduced considerably in the corner region where the flow is influenced by the presence of a second wall; however, it holds accurately in the mid-wall region up to about $z^+ = 1000$.

4.5. *Reynolds stresses*

Although all Reynolds stresses except $\rho\overline{vw}$ were measured at the three Reynolds numbers, since the data were similar, only the results for Re = 53 000 are presented in this paper. Measurements of $(\overline{v^2})^{\frac{1}{2}}$, $(\overline{w^2})^{\frac{1}{2}}$, $\overline{uv}$ and $\overline{uw}$ were corrected for tangential cooling effects as suggested by Lawn (1969). The absolute accuracy of the experimental data is

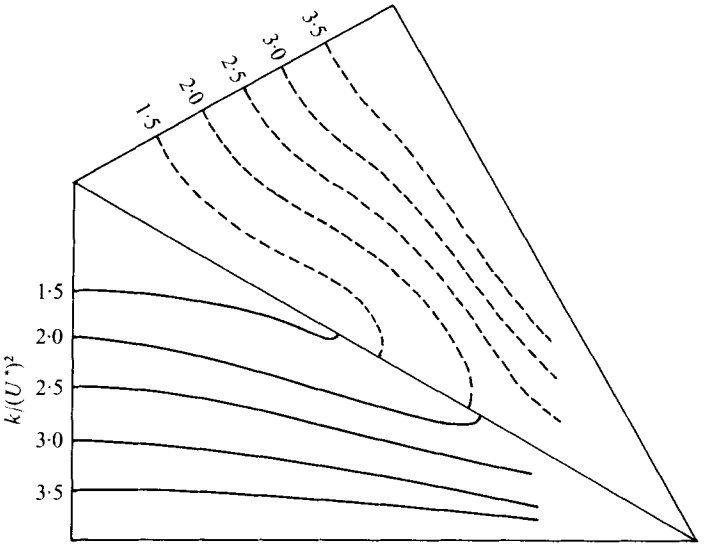

FIGURE 13. Comparison of measured (——) and predicted (- - - -) k. Re = 53000.

not known; however, based on repeatability,† it is estimated that trend line accuracies are within about 3 % for the normal stresses and about 10 % for $\overline{uw}$. No figure is offered for $\overline{uv}$ as its values were very small over much of the flow cell, and its measurement was found to be very sensitive to probe alignment, channel match and wire cleanliness.

Contour plots of constant normal stresses and mean turbulent kinetic energy are presented in figures 10–13, where the results have been normalized by the average friction velocity. These plots clearly indicate the effects of convection of turbulent kinetic energy by secondary flows. In general, as is usual, turbulence levels are highest near the wall where the turbulence is produced and lowest near the duct centreline. But distortions similar to the bulges observed in the mean velocity field are evident. The low turbulence region extends far into the corner while the high turbulence region bulges outwards from the mid-point of the wall, thereby indicating a clockwise circulation of secondary flow.

In figure 14, a comparison of the distributions of $(\overline{u^2})^{\frac{1}{2}}/u^*$, $(\overline{v^2})^{\frac{1}{2}}/u^*$ and $(\overline{w^2})^{\frac{1}{2}}/u^*$ along the mid-wall bisector is given. It is clear that velocity fluctuations parallel to the wall generally exceed those normal to the wall, although the two components have equal magnitudes in the central region of the duct. The latter considered in conjunction with the circular shape of the contours of constant $(\overline{v^2})^{\frac{1}{2}}/u^*$ and $(\overline{w^2})^{\frac{1}{2}}/u^*$ near the duct axis indicates that there is a small core region in which the transverse velocity fluctuations are essentially independent of orientation. This feature is consistent with the results of Laufer (1954) for pipe flow and the measurements of Brundrett & Baines (1964) for a square duct. The distributions of turbulent kinetic energy along normals to the wall are compared further with pipe and square-duct flows in figure 15. In the

† Of the same probe or different probes or combinations thereof. For example, during the course of the work, at least five separate measurements were made of $(\overline{u^2})^{\frac{1}{2}}/u^*$ using three different probe types.

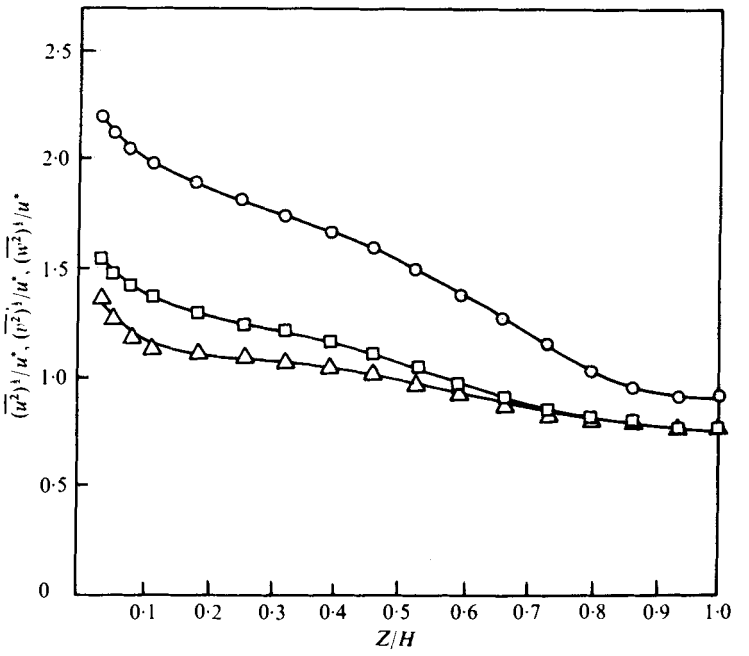

FIGURE 14. Turbulence intensities along mid-wall bisector. Re = 53000.
○, $(\overline{u^2})^{\frac{1}{2}}/u^*$; □, $(\overline{v^2})^{\frac{1}{2}}/u^*$; △, $(\overline{w^2})^{\frac{1}{2}}/u^*$.

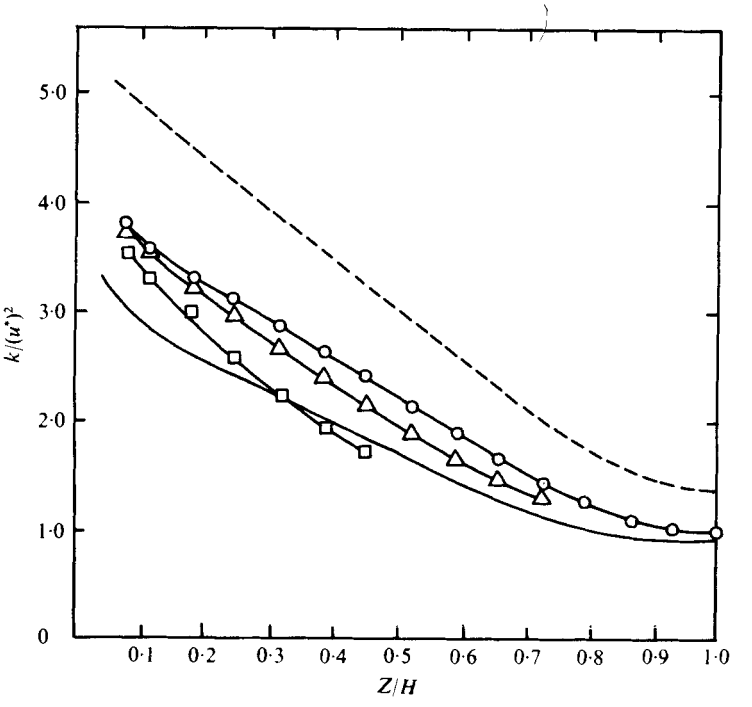

FIGURE 15. Distributions of $k/(u^*)^2$ normal to wall. Present experimental data, Re = 53000: ○, y/L = 0·0; △, y/L = 0·273; □, y/L = 0·41. ——, pipe flow, Laufer (1954), Re = 41000; · · · ·, square duct, Brundrett & Baines (1964), Re = 83000.

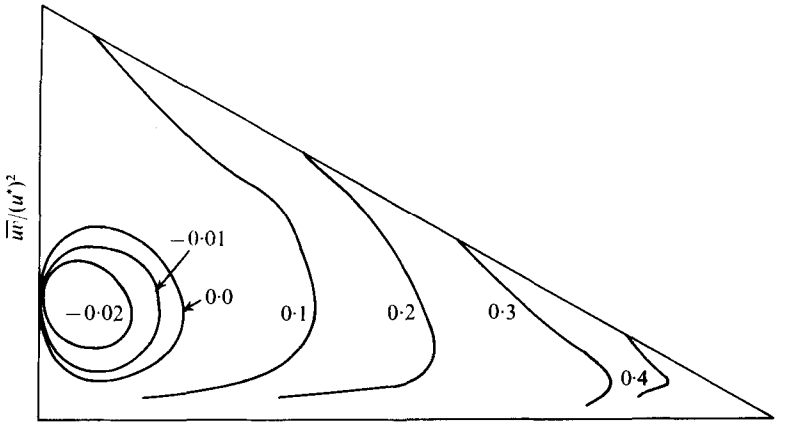

FIGURE 16. Contour plot of $\overline{uv}/(u^*)^2$ distribution. Re = 53000.

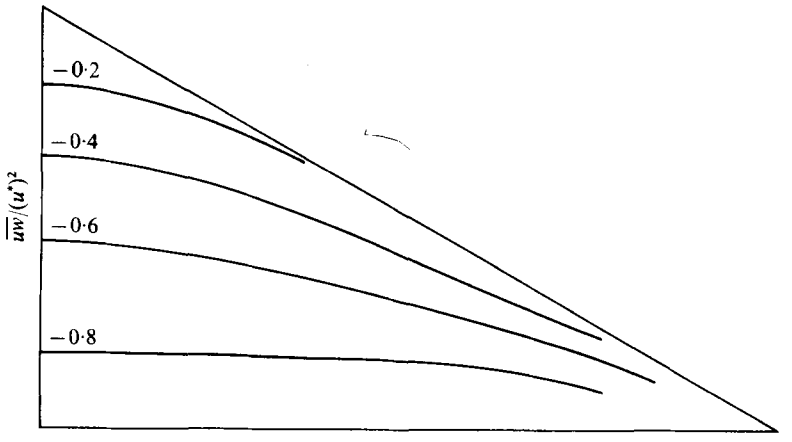

FIGURE 17. Contour plot of $\overline{uw}/(u^*)^2$ distribution. Re = 53000.

central region, the normalized values are generally somewhat higher than for pipe flow but lower than for a square duct.

Concerning the two measured shear stresses, the contours of $\overline{uv}$ presented in figure 16 show that $\overline{uv}$ was generally smallest in the mid-wall region and largest in the corner region and along the corner bisector. An unusual feature of the distribution is the region of small negative $\overline{uv}$ near the mid-wall bisector. Although these negative values are conceded to be comparable in magnitude to the precision limit, repeated measurements consistently indicated a distinct sign change when the probe entered this region. Brundrett & Baines (1964) observed that the corresponding stress in the square-duct flow also changes sign within a primary flow cell. The existence of a negative region is consistent with the concept of a positive turbulent (eddy) viscosity since $\partial \overline{U}/\partial y$ is positive here (owing to secondary flow action – see figure 8) whereas it is negative elsewhere and zero on the mid-wall bisector. It is also noted that measurements showed that $\overline{uv}$ (like $\overline{V}$) has an antisymmetric† distribution about the z axis.

† Of course, if the X-probe is rotated 180° upon passing through the boundary into the adjoining flow cell, then $\overline{uv}$ appears symmetric (as would $\overline{V}$) since the y direction is effectively reversed.

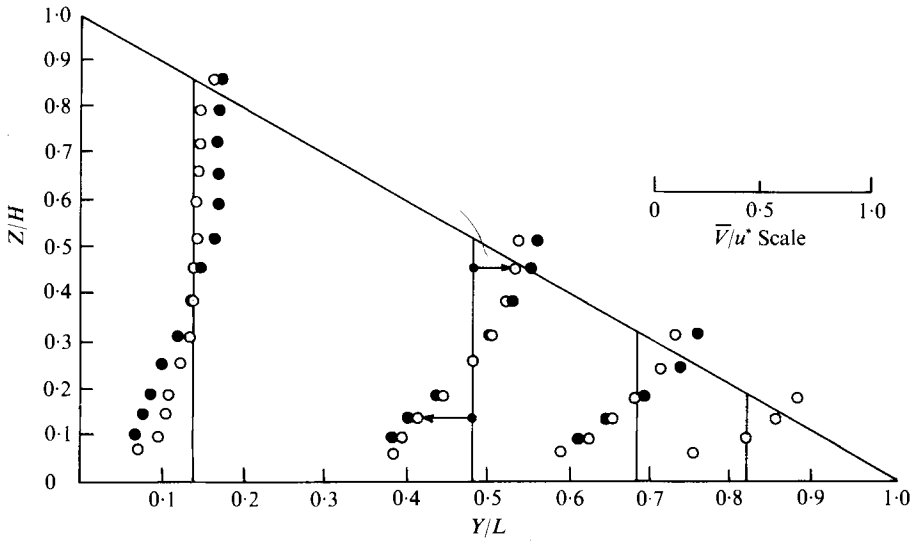

FIGURE 18. Comparison of $\overline{V}$ measured by X-probe (●) and slanted-wire probe (○) at different vertical planes. Re = 53000.

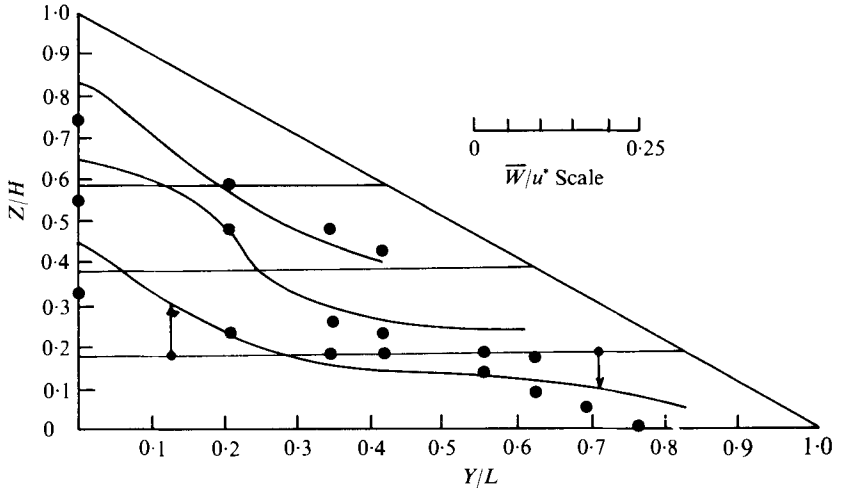

FIGURE 19. Measured (●, X-probe) and predicted (——) $\overline{W}$ distributions at different horizontal planes. Re = 53000.

It is therefore logical that $\overline{uv}$ be zero on the mid-wall bisector, and this was basically substantiated by the measurements.

Contour plots of $\overline{uw}$ are shown in figure 17. The distribution is basically as expected. It may be noted that z direction gradients in $\overline{uw}$ are much larger in the corner region than in the mid-wall region. Gerrard (1976) has examined the x momentum balance [equation (3)] along the mid-wall bisector. The $\overline{uw}$ gradient was found to be dominant in the central region of the duct. The pertinent $\overline{uv}$ gradient also contributed significantly to the balance here. However, nearer the wall, the predominant term was indicated to be convection of axial momentum by $\overline{W}$.

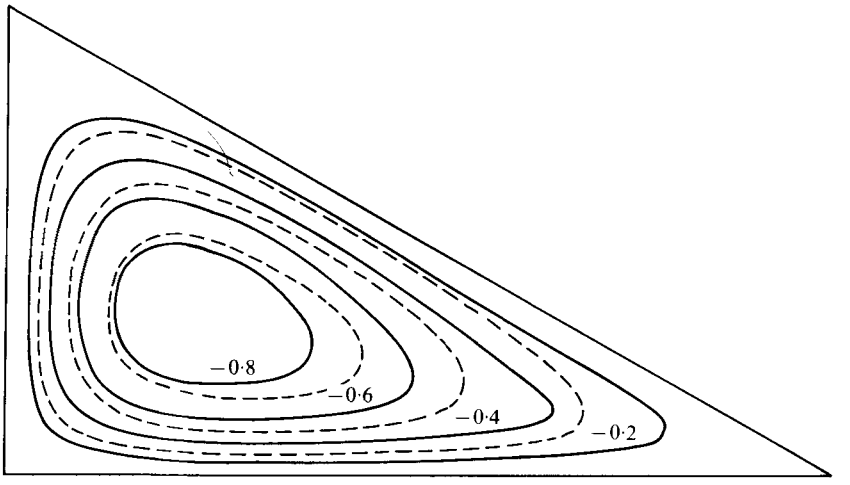

FIGURE 20. Contour plots of predicted stream function distribution. Re = 53000. ——, full source; - - - -, shear suppressed. Values shown are $\psi \times 10^3$.

4.6. *Secondary velocities*

Measurements of the transverse components of velocity were made only along certain vertical (for $\overline{V}$) and horizontal (for $\overline{W}$) lines rather than at all points in the grid. This was part of a technique whereby rapid measurements could be made which eliminated errors due to relative channel drift of the X-probe. Repeatability was maintained in this manner to within about 15 %. The results for $\overline{V}$ are shown in figure 18. The two probes differed most near the corner bisector. This was probably due to the influence on the two near walls. The results for $\overline{W}$ are shown in figure 19. From this distribution and figure 18, it is evident that the actual secondary flow is a single cell of clockwise rotation. Fluid is directed from the centre of the duct to the corner via a path parallel and adjacent to the corner bisector. The results indicate that the maximum secondary velocity occurs in the return flow along the wall where $\overline{V}$ attains a value of about $1\frac{1}{2}$ % of the bulk velocity. Gerrard (1976) has demonstrated that $\overline{V}$ results at different Reynolds numbers scale satisfactorily on average friction velocity.

5. Predicted results and discussion

5.1. *Vorticity production and stream function*

The results predicted by the computational scheme described earlier are presented and discussed in this section mainly for a Reynolds number of 53000. The stream function distributions given by figure 20 were derived using different vorticity production source terms. In one case, the normal stress term only was applied. In the second case, both normal and shear stress terms were retained. It is evident that the penetration of the contours into the corner is mainly due to the shear stress term. This in turn has a direct effect on secondary velocity magnitudes in the corner region as can be seen in figure 21. Since the agreement between both predictions and the experimental data is generally good elsewhere, this suggests that normal stress vorticity production predominates over most of the duct cross-section, the exception being the corner regions where the shear stress term contributes significantly. This differs from

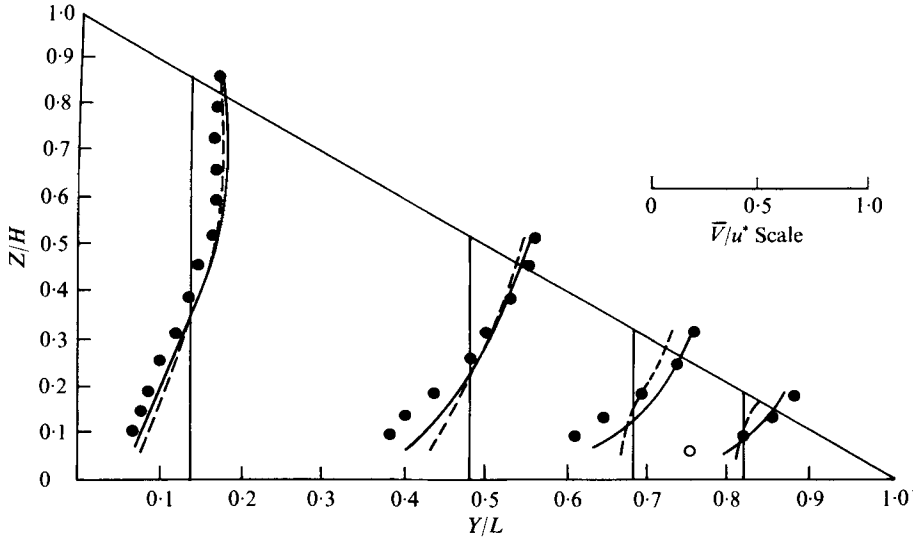

FIGURE 21. Comparison of predicted (——, full source; - - - -, shear suppressed) and measured (●) $\bar{V}$ results. Re = 53000.

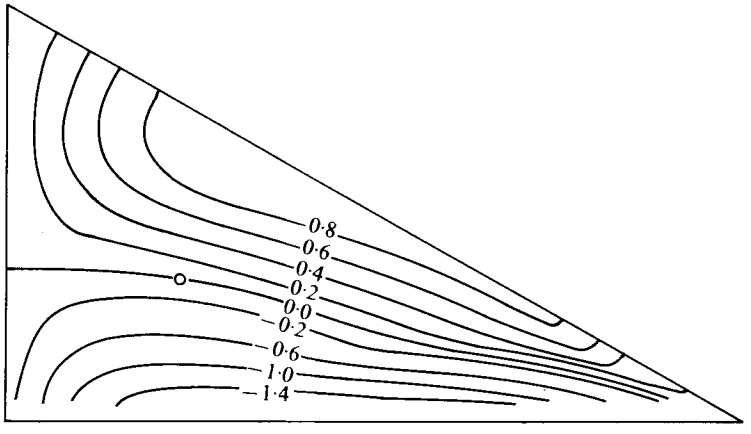

FIGURE 22. Contour plot of predicted $\bar{V}$. Re = 53000. Values shown are $\bar{V}/U_b$ in per cent. ○ indicates centre of secondary flow ($\bar{V}$ = 0 = $\bar{W}$).

the square-duct case where, according to the measurements of Brundrett & Baines (1964), the normal stress term predominates everywhere. All predicted results discussed hereafter were obtained using the full vorticity production source terms.

5.2. *Secondary velocities*

The predicted (full source) secondary velocities are compared with the experimental data† in figure 21 ($\bar{V}$) and figure 19 ($\bar{W}$). The agreement is good except near the wall where in fact the measurement accuracy may have deteriorated owing to wall effect on the probes. Figures 22 and 23 show the predicted results more fully.

† X-probe data except (for $\bar{V}$) for the station nearest to the corner.

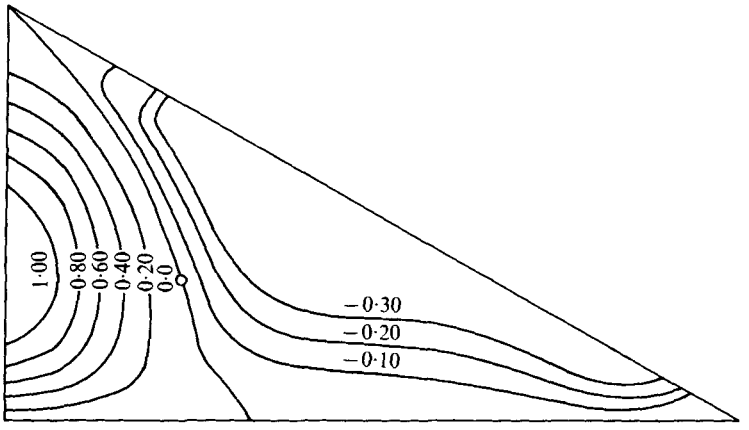

FIGURE 23. Contour plot of predicted $\overline{W}$. Re = 53000. Values shown are $\overline{W}/U_b$ in per cent. ○ indicates centre of secondary flow ($\overline{V} = 0 = \overline{W}$).

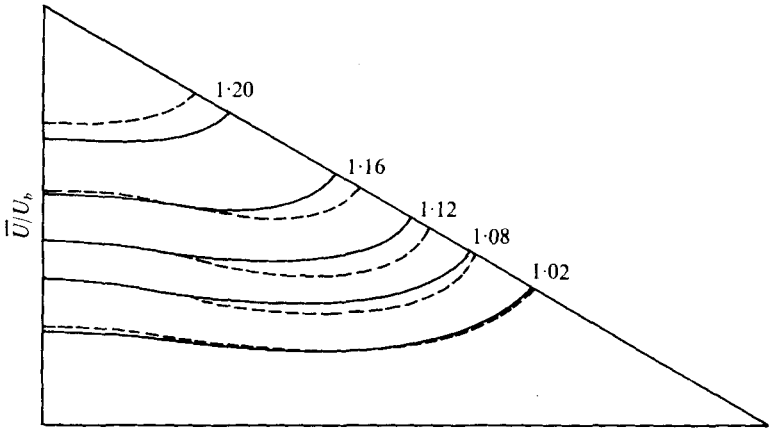

FIGURE 24. Comparison of predicted (- - -) and measured (——) $\overline{U}$ results. Re = 53000. Values shown are $\overline{U}/U_b$.

5.3. *Mean axial velocity distributions*

Figure 24 shows the predicted effect of the secondary flows on the mean axial velocity distribution. The agreement between the predicted and experimental distributions is good when viewed in terms of percentage differences. The contours are almost identical adjacent to the mid-wall bisector except near the duct centreline. The largest discrepancies occur in the core region near the corner bisector. This can be partially attributed to the length scale calculations. An attempt was made to determine the validity of using Buleev's formula for the case of an equilateral triangular duct. The turbulence length scale was calculated from the experimental data on shear stress, turbulent kinetic energy, and axial velocity gradients along the lines $y/L = 0$, and $y/L = 0{\cdot}4$ from the formula

$$l = -\frac{1}{c_\nu (k)^{\frac{1}{2}}} \frac{\overline{uw}}{\partial \overline{U}/\partial z}, \tag{26}$$

with the value of c_ν the same as noted earlier. Comparison of these two distributions with the corresponding ones obtained from Buleev's formula (12) is provided by

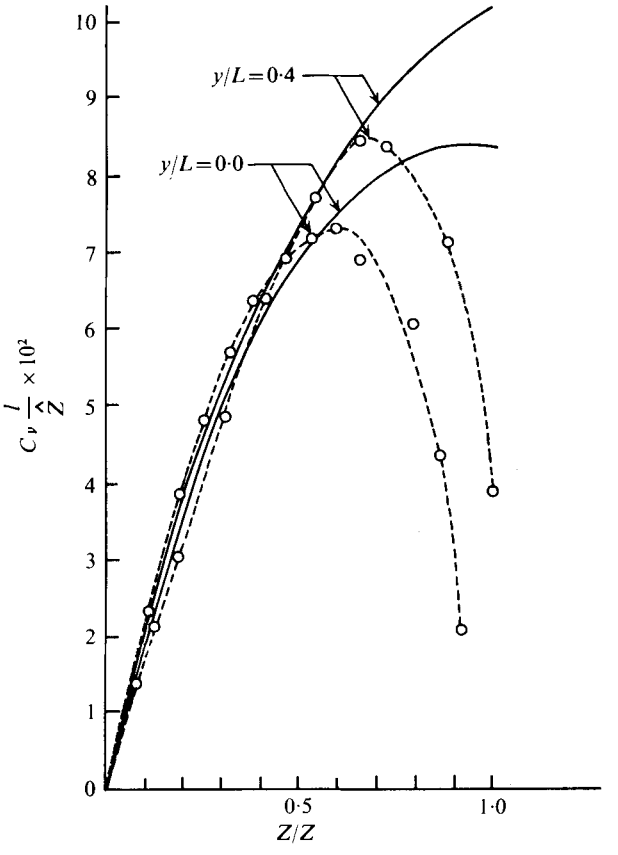

FIGURE 25. Comparison of Buleev's length scale (——) with experimental values (○, - - - -, c_ν = 0·22). Re = 53000.

figure 25 where $\hat{z}$ is the normal distance from the wall to the corner bisector. It is clear that, for the region of $\hat{z}/z > 0{\cdot}6$, (12) tends to overestimate the actual length scale. This means that by using this equation a more flattened axial velocity distribution will result. Nevertheless, despite this minor shortcoming, the authors do not hesitate to recommend employing the Buleev length scale since it produces reasonable results while avoiding experimental input to the prediction technique.

The predicted turbulent kinetic energy field is compared with the experimental contours in figure 13. It is evident that the distortion in these contours is much larger than that of the axial velocity contours. The corresponding situation has also been noted for the square-duct case (Brundrett & Baines 1964; Launder & Ying 1973).

5.4. *Wall shear stress*

The predicted wall shear stress distributions for two Reynolds numbers are superimposed on the experimental results presented in figure 6. The agreement is quite reasonable. The distributions confirm the tendency of secondary flow to equalize the wall shear stress along the wall. It is also of interest to note that, in the case of the equilateral triangular duct, the peak value of the wall shear stress is not displaced as

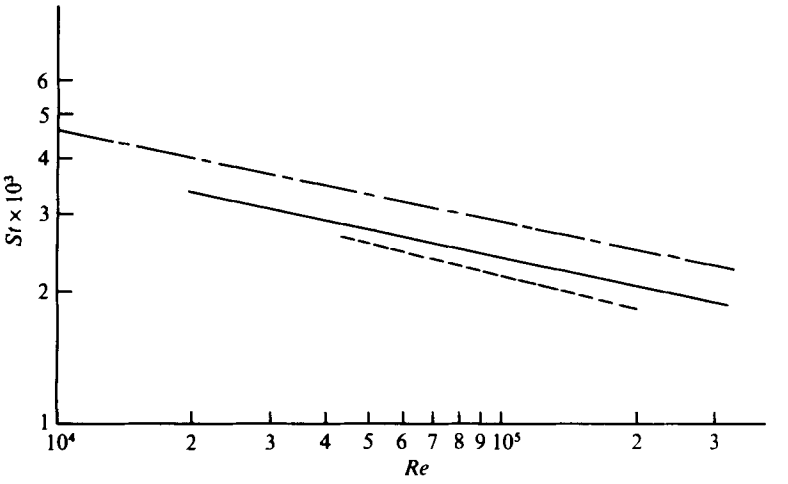

FIGURE 26. Stanton number dependence on Reynolds number. - - - -, equilateral triangular duct, present prediction; ——, square duct, Launder & Ying (1973); — · —, pipe flow, $St = 0{\cdot}023\,(Re)^{-0{\cdot}2}\,(Pr)^{-0{\cdot}67}$, $Pr = 0{\cdot}7$.

far towards the corner as for the square-duct case. For the latter, several investigators have reported that the peak value is located at $y/L \simeq 0{\cdot}5$.

5.5. *Effect of Reynolds number*

Friction factor dependence on Reynolds number was investigated by conducting a series of calculations with full source modelling. The predicted results have been superimposed on figure 5. The predicted friction factors are only slightly below the experimental points. Launder & Ying (1973) observed a similar difference for the square-duct case which they attributed as being probably due to the Buleev method for calculating the length scale distribution in the duct. In any event, both the present prediction and the equation of Malak *et al.* (1975) provide better values of friction factors than the Blasius equation.

The distributions of predicted local wall shear stress (figure 6) do not show any significant tendency towards greater uniformity with increasing Reynolds number as is the case for rectangular ducts (Leutheusser 1963). The present experimental results (figure 6) also do not exhibit Reynolds number dependence over the investigated range.

5.6. *Heat transfer prediction*

As expected, the predicted isotherms within the flow field were qualitatively similar to the predicted pattern for mean axial velocity shown in figure 24. The results are not presented since there are no experimental data for comparison. Figure 26 shows the predicted relationship between Stanton number and Reynolds number and includes, for comparison purposes, data for both square-duct and pipe flow. For a given Reynolds number, the Stanton numbers for the equilateral triangular duct and the square duct are within 10 % of each other over the indicated Reynolds number range. The heat flux distribution around the periphery of the duct had a similar distribution to that of the wall shear stress with a maximum value at $y/L \simeq \frac{1}{3}$. For square ducts, Launder &

Ying (1973) predicted a maximum value of heat flux at $y/L \simeq 0{\cdot}5$, the same position as wall shear stress peaks.

6. Conclusions

The following conclusions are based on the above results and are applicable to fully developed turbulent flows in equilateral triangular ducts for Reynolds numbers in the range 5×10^4 to $1{\cdot}1 \times 10^5$.

(i) The measured and predicted friction factors are 5 % to 6½ % lower than those predicted by the Blasius equation. The 'universal criterion relationship' proposed by Malak *et al.* (1975) provides a satisfactory correlation of the present friction factor data.

(ii) Owing to momentum transport by secondary flows, the wall shear stress over the central half of each wall is constant to within a few per cent.

(iii) The mean axial velocity distribution in the wall region can be described by the inner law of the wall if u^+ and z^+ are based on local values of the wall shear stress.

(iv) The mean axial velocity and turbulence fields are clearly influenced by the presence of secondary flows. The effect on the turbulent kinetic energy field is more pronounced than on the axial velocity field.

(v) The normal Reynolds stress distributions are essentially independent of Reynolds number when normalized by the average friction velocity.

(vi) The secondary flow pattern observed by Nikuradse (1930) was confirmed by direct measurements of the $\overline{V}$ and $\overline{W}$ components. The actual pattern consists of six counter-rotating flow cells in which the flow is directed from the centre of the duct to the corner via the corner bisector. The return flow is along the wall and the wall bisector. The $\overline{V}$ component of the secondary velocity has a maximum strength of about 1½ % of U_b in the return flow along the wall.

(vii) Successful flow predictions without experimental input to the vorticity equation can be achieved by expressing the Reynolds stresses in the plane of the cross-section by gradients in the mean axial velocity. Both normal and shear stress terms must be included in the vorticity production source term in order to provide accurate prediction in the corner region. The Buleev formula for the turbulence length scale is adequate for the equilateral triangular duct provided that the value 0·006 is assigned to c in (10) and (11). The Launder–Ying model provides a useful engineering tool for similar flow problems; the present results increase the prospects of successful flow and heat transfer predictions in rod bundle arrays.

(viii) For the heat transfer situation examined in this paper, the predicted results indicate that equilateral triangular ducts and square ducts have a similar *St–Re* relationship.

The authors gratefully acknowledge the support provided for this research by National Research Council of Canada.

REFERENCES

BANDOPADHAYAY, P. C. & HINWOOD, J. B. 1973 *J. Fluid Mech.* **59**, 775.

BRUNDRETT, E. & BAINES, W. D. 1964 *J. Fluid Mech.* **19**, 375.

BULEEV, N. I. 1963 *A.E.R.E. Translation* no. 957.

CARAJILESCOV, P. & TODREAS, N. E. 1976 *J. Heat Transfer, Trans. A.S.M.E.* **98**, 262.

CARLSON, C. W. & IRVINE, T. F. 1961 *J. Heat Transfer, Trans. A.S.M.E.* **83**, 441.

COPE, R. C. & HANKS, R. W. 1972 *Ind. Engng Chem. Fund.* **11**, 106.

CREMERS, C. J. & ECKERT, E. R. G. 1962 *J. Appl. Mech. Trans. A.S.M.E.* **4**, 609.

DEISSLER, D. G. & TAYLOR, M. F. 1959 *N.A.S.A. Tech. Rep.* R-31.

GERARD, R. 1974 *Proc. A.S.C.E.* **100** (HY3), 425.

GERRARD, A. D. 1976 M.Sc. thesis, University of Manitoba.

GESSNER, F. B. & JONES, J. B. 1965 *J. Fluid Mech.* **23**, 689.

GOSMAN, A. D., PUN, W. M., RUNCHAL, A. K., SPALDING, D. B. & WOLFSHTEIN, M. 1969 *Heat and Mass Transfer in Recirculating Flows.* Academic Press.

GOSMAN, A. D. & PUN, W. M. 1974 *Imperial College Mech. Engng Dept. Rep.* HTS/74/3.

HALL, C. & SVENNINGSSON, P. J. 1971 *AB Atomenergi Rep.* AE-RL-1326.

HINZE, J. O. 1973 *Appl. Sci. Res.* **28**, 453.

HOAGLAND, L. C. 1960 Ph.D. thesis, M.I.T.

JAYATILLEKE, C. L. V. 1969 *Prog. Heat Mass Transfer* **1**, 193.

KACKER, S. C. 1973 *J. Fluid Mech.* **57**, 583.

KJELLSTROM, B. & STENBACK, A. 1970 *AB Atomenergi Rep.* AE-RV-145.

KOKOREV, L. S., KORSUN, A. S., KOSTYUNIN, B. N., PETROVICHEV, V. I. & STRUENZE, R. L. 1971 *Heat Trans.-Soviet Res.* **3** (1), 66.

LAUFER, J. 1954 *N.A.C.A. Rep.* no. 1174.

LAUNDER, B. E. & SINGHAM, J. R. 1971 *Symp. Internal Flow, Univ. Salford*, paper 12.

LAUNDER, B. E. & YING, W. M. 1972 *J. Fluid Mech.* **54**, 289,

LAUNDER, B. E. & YING, W. M. 1973 *Proc. Inst. Mech. Engrs* **187**, 455.

LAWN, C. J. 1969 *C.E.G.B. Berkeley Nucl. Lab. Rep.* RD/B/M 1277.

LEUTHEUSSER, H. J. 1963 *Proc. A.S.C.E.* **89** (HY3), 1.

LIGGETT, J. A., CHIU, C. & MIAO, L. S. 1965 *Proc. A.S.C.E.* **91** (HY6), 99.

LYALL, H. G. 1971 *Symp. Internal Flows, Univ. Salford*, paper 33.

MALAK, J., HEJNA, J. & SCHMID, J. 1975 *Int. J. Heat Mass Transfer* **18**, 139.

NIKURADSE, J. 1926 *V.D.I. Forsch.* 281.

NIKURADSE, J. 1930 *Ingenieur-Archiv* **1**, 306.

OWER, F. & PANKHURST, R. C. 1966 *The Measurement of Air Flow.* Pergamon.

PATEL, V. C. 1965 *J. Fluid Mech.* **23**, 185.

ROGERS, J. T. & TAHIR, A. E. E. 1975 *A.S.M.E. Paper* no. 75-HT-31.

ROWE, D. S., JOHNSON, B. M. & KNUDSEN, J. G. 1974 *Int. J. Heat Mass Transfer* **17**, 407.

TRACEY, H. J. 1965 *Proc. A.S.C.E.* **91** (HY6), 9.

TRUPP, A. C. & AZAD, R. S. 1975 *Nucl. Engng Des.* **32**, no. 1, 47.

WILSON, N. W., AZAD, R. S. & TRUPP, A. C. 1971 *Symp. Internal Flows, Univ. Salford*, paper 11.